

Stepwise Subduction Observed at a Front in the Marginal Ice Zone in Fram Strait



Key Points:

- We present a study of temporally and spatially highly resolved observations of a front system near the ice edge
- We observe no mixed layer and the ocean is stratified up to the surface
- We propose that subduction occurs stepwise along surface meltwater fronts and subsurface fronts separating Polar Water and Atlantic Water

Correspondence to:

Z. Hofmann,
zerlina.hofmann@awi.de

Citation:

Hofmann, Z., von Appen, W.-J., Kanzow, T., Becker, H., Hagemann, J., Hufnagel, L., & Iversen, M. H. (2024). Stepwise subduction observed at a front in the marginal ice zone in Fram Strait. *Journal of Geophysical Research: Oceans*, 129, e2023JC020641. <https://doi.org/10.1029/2023JC020641>

Received 26 OCT 2023

Accepted 19 MAR 2024

Author Contributions:

Conceptualization: Zerlina Hofmann, Wilken-Jon von Appen, Torsten Kanzow, Morten H. Iversen

Data curation: Zerlina Hofmann, Hauke Becker, Morten H. Iversen

Formal analysis: Zerlina Hofmann, Wilken-Jon von Appen, Lili Hufnagel, Morten H. Iversen

Funding acquisition: Wilken-Jon von Appen, Torsten Kanzow, Morten H. Iversen

Investigation: Zerlina Hofmann, Wilken-Jon von Appen, Hauke Becker, Jonas Hagemann, Lili Hufnagel, Morten H. Iversen


Methodology: Zerlina Hofmann, Wilken-Jon von Appen, Hauke Becker, Jonas Hagemann, Lili Hufnagel, Morten H. Iversen

Project administration: Wilken-Jon von Appen, Torsten Kanzow, Morten H. Iversen

Resources: Wilken-Jon von Appen, Torsten Kanzow, Hauke Becker

© 2024. The Authors.

This is an open access article under the terms of the [Creative Commons Attribution License](https://creativecommons.org/licenses/by/4.0/), which permits use, distribution and reproduction in any medium, provided the original work is properly cited.

Zerlina Hofmann¹ , Wilken-Jon von Appen¹ , Torsten Kanzow^{1,2} , Hauke Becker¹, Jonas Hagemann¹ , Lili Hufnagel^{1,3}, and Morten H. Iversen^{1,3} 

¹Alfred Wegener Institute, Helmholtz Centre for Polar and Marine Research, Bremerhaven, Germany, ²Department of Physics and Electrical Engineering, University of Bremen, Bremen, Germany, ³Center for Marine Environmental Sciences (MARUM), University of Bremen, Bremen, Germany

Abstract At high latitudes, submesoscale dynamics act on scales of $\mathcal{O}(100\text{ m}–1\text{ km})$ and are associated with the breakdown of geostrophic balance, vertical velocities, and energy cascading to small scales. Submesoscale features such as fronts, filaments, and eddies are ubiquitous in marginal ice zones forced by the large horizontal density gradients. In July 2020, we identified multiple fronts and filaments using a towed undulating vehicle near the sea ice edge in central Fram Strait, the oceanic gateway to the Arctic Ocean between Greenland and Svalbard. Sea ice covered the entire study region 1–2 weeks earlier, and a stratified meltwater layer was present. We observed a front between warm and saline Atlantic Water (AW) and cold and fresh Polar Water (PW) at 30–85 m depth, where we identified a subsurface maximum in chlorophyll fluorescence and other biogeochemical properties extending along the tilted isopycnals down to 75 m, indicating subduction of AW (mixed with meltwater) that had previously occurred. The meltwater layer also featured multiple shallow fronts, one of which exhibited high velocities and a subsurface maximum in chlorophyll fluorescence, possibly indicating subduction of PW below the meltwater layer. The fronts at different depth levels suggest a stepwise subduction process near the ice edge, where water subducts from the surface below the meltwater and then further down along subsurface fronts. The submesoscale features were part of a larger-scale mesoscale pattern in the marginal ice zone. As sea ice continuously retreats, such features may become more common in the Arctic Ocean.

Plain Language Summary Submesoscale dynamics are small-scale (100 m–1 km) horizontal and vertical flows that create fronts and whirls. These features are typical in the transition from open ocean to sea ice. In the summer of 2020, we observed multiple fronts near the sea ice edge in central Fram Strait. Fram Strait is the oceanic gateway between the Atlantic Ocean and the Arctic Ocean. At the time, fresh meltwater covered the area. Below the meltwater layer, we observed a front between warm and saline Atlantic Water (AW) and cold and fresh Polar Water (PW). The amount of fluorescence (a measure of biomass) observed below the PW showed that AW moved downwards. Prior observations show that AW is in touch with the sea surface in the eastern part of Fram Strait. Our observations thus suggest a step-by-step process happening near the ice edge. AW moves from the surface below the meltwater in the first step and down below PW in the second step. This process can increase the vertical transport of biological material (i.e., carbon) near the ice edge in summer. The vertical transport is part of the global carbon cycle.

1. Introduction

Submesoscale phenomena in the ocean such as eddies, density fronts, and filaments exhibit order one Rossby numbers ($Ro = \frac{U}{Lf}$, with U , L characteristic velocity and length scales, f Coriolis parameter). $Ro = 1$ corresponds to length scales of 0.1–10 km (0.1–1 km at higher latitudes) and time scales of hours to days (e.g., Mahadevan, 2016). The submesoscale bridges the energy cascade gap between the quasi-geostrophic mesoscale (at length scales $>10\text{ km}$) and three-dimensional processes (at length scales $<100\text{ m}$), where diapycnal mixing can occur (Thomas et al., 2008). Breakdown of geostrophic balance leads to the evolution of ageostrophic secondary circulations (ASCs), characterized by large vertical velocities with $\mathcal{O}(10–100\text{ m day}^{-1})$ as revealed by observations in the subtropics (e.g., Hosegood et al., 2017), mid-latitudes (e.g., Johnson et al., 2020), the Arctic (e.g., von Appen et al., 2018), and in numerical models (e.g., Manucharyan & Thompson, 2017). As part of the ASC, water is removed from an upper layer of a denser water mass and moved vertically and horizontally below a lighter water mass, thus contributing to restratification and restoring of the cross-front geostrophic balance

Software: Hauke Becker
Supervision: Wilken-Jon von Appen, Torsten Kanzow, Morten H. Iversen
Visualization: Zerlina Hofmann
Writing – original draft: Zerlina Hofmann
Writing – review & editing: Zerlina Hofmann, Wilken-Jon von Appen, Torsten Kanzow, Lili Hufnagel, Morten H. Iversen

(McWilliams et al., 2009). This process is referred to as subduction, which influences turbulent lateral and vertical mixing (e.g., Koenig et al., 2020), nutrient fluxes and primary productivity (Mahadevan, 2016), biodiversity (Lévy et al., 2018), particulate organic carbon (POC) export (e.g., Omand et al., 2015), and biogeochemical reactions (Martin et al., 2015).

In this study, we focus on submesoscale processes in Fram Strait, the oceanic gateway to the Arctic Ocean between Greenland and Svalbard, where warm and saline Atlantic Water (AW) interacts with sea ice and cold and fresh Polar Water (PW). AW, transported from lower latitudes via the North Atlantic Current and the Norwegian Atlantic Current (Hansen & Østerhus, 2000), continues as the West Spitsbergen Current (WSC, red in Figures 1a and 1b) along the shelf break west of Svalbard, carrying heat into the Arctic Ocean (Beszczynska-Möller et al., 2012). PW exits the Arctic Ocean via the East Greenland Current (EGC, blue in Figures 1a and 1b) along the shelfbreak east of Greenland (Håvik et al., 2017), contributing to the Nordic Seas' overflow waters and the Meridional Overturning Circulation (Våge et al., 2013). In Fram Strait, AW "recirculates" (i.e., moves westward) along two pathways affected by extensive eddy activity (Hofmann et al., 2021). Once it encounters lighter PW or the sea ice edge in central Fram Strait, it subducts (Hattermann et al., 2016). The transition from the open ocean to pack ice, the marginal ice zone (MIZ), is characterized by low to intermediate concentrations of mobile sea ice and exhibits high temporal and spatial variability. With declining Arctic sea ice extent and thickness (Parkinson & DiGirolamo, 2021), the MIZs in the Arctic Ocean are undergoing changes, with observed trends of widening in the summer and narrowing in the winter (Strong & Rigor, 2013), and more energetic eddies and amplified ocean-ice heat exchange (Manucharyan & Thompson, 2022). Recent satellite observations indicate that submesoscale and small mesoscale eddies dominate the eddy field of the MIZ in Fram Strait and are primarily detected where the ice concentration is below 20%, with twice as many cyclonic eddies occurring as anticyclonic eddies (Kozlov & Atadzhanova, 2022). Cyclonic submesoscale eddies can trap sea ice, advect it over warmer water, and increase melt (Manucharyan & Thompson, 2017).

Considering the impact of sea ice in the MIZ on the ecosystem, von Appen, Waite, et al. (2021) differentiate between two regimes regarding the impact on the biological carbon pump: the presence of a highly stratified surface layer, which is frequently present near the sea ice edge in summer due to sea ice melt (dubbed the "meltwater regime") and the presence of a mixed layer more typical of the open ocean (dubbed the "mixed-layer regime"). Thus, the presence of sea ice but also that of a stratified surface layer plays a role in the vertical export of biological matter and submesoscale processes. Aside from dissolved inorganic and organic carbon (Lévy et al., 2013), particulate organic carbon (POC) is transported downwards along with the subduction of water masses (Stukel et al., 2018). Slow-sinking and non-sinking organic material, such as phytoplankton or aggregates, have been observed to be exported by filament and eddy structures down to 350 m depth (Llort et al., 2018;

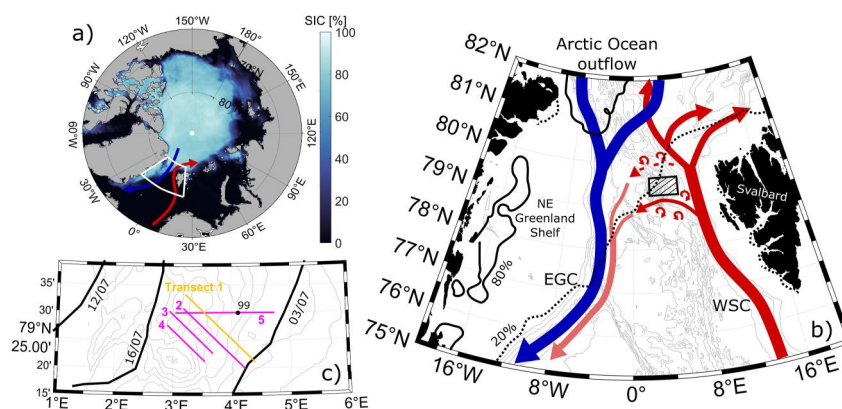


Figure 1. (a) Map of the Arctic Ocean with mean sea ice concentration (SIC) [%] in July 2020, and schematic circulation. (b) Map of Fram Strait with bathymetry from Schaffer et al. (2019). The more detailed schematic circulation includes the Arctic Ocean outflow (blue), the northward inflow of the West Spitsbergen Current (WSC, red), its recirculating westward flow (red), and the southward flow of the East Greenland Current (EGC, blue). SIC as in panel (a). The black hatched box indicates the study region. (c) Study region with the same bathymetry and 20% SIC on 03, 12, and 16 July 2020 (black contours), as well as the transect locations used in this study (magenta), highlighting Transect 1 (orange) and the location of station 99.

Omand et al., 2015). Additionally, physical processes shape the biological processes in Arctic filaments and the associated POC export (von Appen et al., 2018; Fadeev, Wietz, et al., 2021). The magnitude of the POC flux in the Arctic depends on the ice cover and the dominating phytoplankton community (e.g., Arrigo et al., 2012). Higher carbon flux is observed in diatom-dominated regions, while areas dominated by the prymnesiophyte *Phaeocystis* lead to less carbon export (Dybwad et al., 2021; Fadeev, Rogge, et al., 2021).

Regarding simulations of submesoscale processes, earlier studies emphasized the significance of model resolution in accurately representing vertical motion (e.g., Mahadevan & Tandon, 2006). Recent advancements in box models (e.g., Aravind et al., 2023; Cornejo & Bahamonde, 2023) and Lagrangian trajectory modeling (Freilich & Mahadevan, 2021; Mahadevan et al., 2020) have improved the understanding of submesoscale processes far beyond the simple Eady model proposed by Eady (1949). However, computational limitations in Earth System Models or General Circulation Models often prevent the resolution of submesoscale or even mesoscale processes and often assume hydrostatic and geostrophic relationships. Lack of resolution necessitates parameterizations, even though they significantly affect the mean state of the ocean and climate variability in the models compared to explicitly representing (sub-)mesoscale processes (Hewitt et al., 2020). Parameterizations have been (e.g., Fox-Kemper et al., 2008) and are still under development (e.g., Bodner et al., 2023; Yankovsky et al., 2021; Zhang et al., 2023). Alternative modeling options include high-resolution nests or running the model at a lower resolution during spin-up and then at a higher resolution for an analysis period (e.g., Bashmachnikov et al., 2020; Manucharyan & Thompson, 2022).

Observing submesoscale processes at fronts in the upper ocean poses challenges due to their rapid evolution and variability on scales not easily captured by standard observational methods, particularly in the Arctic, where the mesoscale Rossby radius of deformation is only between 2 and 6 km (Zhao et al., 2014; von Appen et al., 2016), and submesoscale processes occur within hours to days. Coordinated surveys employing multiple instruments, including satellite observations, are typically necessary for comprehensive observation. Studies in the Arctic include underway conductivity-temperature-depth (UCTD) surveys (von Appen et al., 2018; Brenner et al., 2020) and autonomous underwater vehicle surveys (Koenig et al., 2020; Tippenhauer et al., 2021; Wulff et al., 2016). Studies from the Southern Ocean are, for example, Giddy et al. (2021); du Plessis et al. (2022), utilizing gliders. Some examples of studies from other regions of the world are Hosegood et al. (2017), Mahadevan et al. (2020), Archer et al. (2020), von Appen et al. (2020), with the two latter employing towed undulating systems. Most of these studies additionally utilized a variety of instruments, such as a vessel-mounted Acoustic Doppler Current Profiler (ADCP), a thermosalinograph, a conductivity-temperature-depth (CTD) rosette, water sampling, atmospheric observations, and reanalysis or model data. The survey durations ranged from a few hours (Archer et al., 2020; Tippenhauer et al., 2021; Wulff et al., 2016) to 1–1.5 days (von Appen et al., 2018; Brenner et al., 2020; Koenig et al., 2020; von Appen et al., 2020), with more comprehensive studies such as Hosegood et al. (2017), Mahadevan et al. (2020), Giddy et al. (2021), du Plessis et al. (2022), lasting up to multiple weeks or months. The surveys primarily targeted the upper ocean (down to 50–350 m) with a horizontal resolution of 100–1,000 m (except for Hosegood et al. (2017), Archer et al. (2020), von Appen et al. (2020), Giddy et al. (2021), du Plessis et al. (2022), which were conducted at lower latitudes and thus deemed a lower resolution sufficient). Satellite observations can be of use to identify the approximate location of the front, followed by confirmation using the thermosalinograph. Surfactants like surface drifters (D'Asaro et al., 2018), plastics (Wang et al., 2022), or sea ice in the MIZ (von Appen et al., 2018) can act as indicators for areas of convergence and enhanced vertical velocities and enable longer study periods, yet they do not reveal water mass or biological properties. Ideally, studies incorporate not only temperature, salinity, and velocity measurements but also biogeochemical parameters and biological samples to act as additional tracers to highlight physical processes and study the effects on the ecosystem. Conducting such studies that also resolve the submesoscale requires significant effort. Hence, they are often either short, focused on a single transect, or lack diversity of measurement types. The study discussed here lasted 11 days and aims to accommodate a multitude of measurements at the high resolution required to resolve submesoscale processes in the Arctic.

We start this paper by describing the data and methods we use (Section 2). We then analyze a single transect in detail (Section 3.1) and discuss its main features in terms of water masses, flow direction, and subduction of biological material. Based on additional transects, we put our findings in a (sub-)mesoscale spatial context (Section 3.2). We further discuss the process of subduction near the MIZ associated with a stratified meltwater layer near the surface (Section 4.1) and how the mesoscale embeds the submesoscale in the MIZ (Section 4.2) before concluding our findings (Section 5).

2. Data and Methods

We acquired shipboard data during cruise MSM93 of RV *Maria S. Merian* from 05 to 16 July 2020 (von Appen, 2021). The study area (Figure 1b, black hatched box) is located in central Fram Strait in the MIZ, between 79°15'N and 79°35'N, 2°45'E and 4°45'E, coincidentally near the Molloy Hole at 79°8'N, 2°49'E. For one and a half weeks, we conducted a process study at the interface of AW and PW near the ice edge. We utilize five transects in this study, numbered 1–5 (see Figure 1c), which we conducted on the night of 14/15 July. We mainly focus on one of the occupations of Transect 1. We conducted these observations specifically between 15:29 and 17:28 UTC on 14 July 2020 using the Triaxus towed vehicle between 5 and 100 m water depth, at submesoscale resolving scales. Additionally, we use satellite observations and reanalysis data during the time of the in situ observations to add spatial information.

2.1. Shipboard Data

Vessel Mounted Acoustic Doppler Current Profiler (VMADCP): To measure ocean velocity, we used the 75 kHz Teledyne RD Instruments vessel-mounted ADCP, mounted in the hull of RV *Maria S. Merian* at 6.5 m depth. We process the data with the Ocean Surveyor Sputum Interpreter software, version 1.9, developed by GEOMAR. We average the 8 m vertical bins between 18.5 and 410.5 m over 60 s. We remove the first bin due to unrealistically high velocities, so measurements are available between 26.5 and 410.5 m.

We disregard tides here, and consequently do not detide the velocity measurements, as tides are mainly barotropic in the study region (deep ocean) and are thus not associated with vertical velocity gradients. They would have only influenced horizontal gradients if our observations had lasted longer than one tidal period, which is not the case for individual transects. The set of transects discussed in Section 3.2 took 12 hr to acquire. Nevertheless, tides are generally of small amplitude in this region—about one order of magnitude smaller than our velocity observations, according to the Arctic Ocean Inverse Tide Model (Padman & Erofeeva, 2004; Padman et al., 2020).

Triaxus towed vehicle: The MacArtney TRIAXUS E (extended version) is a 1.95 m wide, 1.25 m tall, and 1.85 m long remotely operated towed vehicle, which was towed behind RV *Maria S. Merian* at a speed of ~5–6 knots (2.5–3 m s⁻¹) while auto-undulating in a sawtooth-pattern between 5 and 100 m at a vertical speed of 1 m s⁻¹, with an average horizontal resolution of 275 m.

Of the sensors mounted on the Triaxus, we use dual SeaBird SBE911+ temperature and conductivity sensors, a WETLabs ECO fluorometer and transmissiometer, an SBE43 dissolved oxygen sensor, a Satlantic photosynthetically available radiation sensor, and a Seabird Deep SUNA nitrate sensor. Chlorophyll *a* fluorescence was corrected by an offset of 0.16 μg L⁻¹. To georeference the Triaxus measurements, the length of the towing cable is considered, as well as the relative position of the individual sensors on the Triaxus. We correct the time lag stemming from the differences in different sensors. We filter the data with a 0.5 s (12 measurements) low pass filter and subsequently interpolate them to a 0.5 s grid. We then identify upcasts and downcasts as times when the absolute vertical velocity of the CTD was >0.5 m s⁻¹ and grid them to 0.5 m vertical bins. Optical nitrate data is corrected with an offset of +4.5 μmol L⁻¹, to avoid negative values and have maximum values in line with known observations (e.g., Tuerena et al., 2021).

Data Gridding: The underway measurements from VMADCP and Triaxus along transects are gridded with the minimum curvature under tension method (Smith & Wessel, 1990). The resulting gridded data for each transect has a vertical resolution of 5 m that extends from 5 to 100 m and a horizontal resolution of 0.5 km.

Surface drifters: Southtek Iridium Global Positioning System (GPS) drifters with a 30 cm PVC drogue recorded GPS positions every 10 min, from which we calculate surface ocean velocities. We deployed them with a constant spacing of 2 km along transects (see Figure 4 for deployment locations, magenta crosses), 21 drifters from 10 July 19:40 to 11 July 01:30 UTC and 10 drifters from 13 July 03:30 to 05:20 UTC.

Shipboard CTD-rossette: Vertical profiles of temperature, salinity, and chlorophyll *a* fluorescence were acquired with a standard dual sensor Seabird 911+ CTD with an additional WETLabs ECO fluorometer, mounted on a rosette. We process the data with standard routines of the Sea-Bird-Electronics Data Processing software.

In-situ camera for aggregates: The vertical particle distribution was recorded with a remotely observing in-situ camera for aggregates system (ROSINA) at selected stations. The camera system was lowered with a speed of

0.3 m s⁻¹ and acquired two images per second, with a sampling volume of 82.2 mL. The acquired images are processed using OpenCV image processing software, which searches for the particle contours.

Ship weather station: 10 m wind direction and velocity was measured by the on-board automatic weather station of RV *Maria S. Merian*.

2.2. Derived Variables

We calculate the conservative temperature Θ and the absolute salinity S_A based on the Gibbs SeaWater (GSW) Oceanographic Toolbox of the Thermodynamic Equations Of Seawater (TEOS)-10 from gridded temperature, salinity, and pressure (McDougall & Barker, 2011), and the potential density anomaly σ based on the SeaWater library of Equation Of State Of Seawater (EOS)-80 (Nayar et al., 2016) from gridded temperature, salinity, and pressure.

The horizontal buoyancy gradient M^2 is calculated with $M^2 = -\frac{g}{\rho_0} \frac{\partial \rho}{\partial x}$, where $g = 9.83 \text{ m s}^{-2}$, and $\rho_0 = 1.028 \text{ kg m}^{-3}$. Geostrophic velocity v_g is calculated with $\int \frac{g}{\rho_0 f} \rho dx$, where f is the Coriolis parameter. We assume a level of no motion of 100 m depth. The euphotic depth is estimated by calculating the depth, to which 1% of the light at the surface can reach.

The calculation of horizontal gradients for individual transects is only possible along the ship track, that is, along-transect ($\frac{\partial}{\partial x}$). However, since we conducted multiple parallel transects within a time frame that we consider submesoscale-resolving (i.e., time scales of hours to days), we can also calculate across-transect gradients ($\frac{\partial}{\partial y}$), albeit at a lower spatial resolution. With the help of in situ measurements such as velocity measurements of the VMADCP and the surface drifters, and previously conducted transects with the Triaxus or the UCTD, we aimed to conduct our transects across-front. Analysis of the spatial distribution of the frontal systems suggests the fronts examined in Transect 1 are reasonably perpendicular to the transects (for further analysis, see Section 3.2). Along-front gradients ($\frac{\partial}{\partial y}$) are typically much smaller than across-front gradients ($\frac{\partial}{\partial x}$). For our measurements, the along-front buoyancy gradient, for example, is one order of magnitude smaller than the across-front buoyancy gradient. We calculate all gradients as a centered difference.

To determine water mass fractions, we define three water mass end members from the Θ - S_A diagram of the main occupation of Transect 1 (Figure 2e). They are similar to what has been found in central Fram Strait before (e.g., Richter et al., 2018). AW is the most saline water mass ($\Theta = 4.33^\circ\text{C}$ and $S_A = 35.16 \text{ g kg}^{-1}$), PW the coldest water mass ($\Theta = -1.76^\circ\text{C}$ and $S_A = 34.24 \text{ g kg}^{-1}$), and Surface Water (SW) the freshest water mass ($\Theta = 1.28^\circ\text{C}$ and $S_A = 35.81 \text{ g kg}^{-1}$). From the Θ - S_A definition and mass conservation, we determine water mass fractions of AW, PW, and SW for each pair of Θ - S_A measurements. If this leads to negative values, that is, the water is slightly outside the triangle of the three end members, we set the water mass fraction to 0. We treat the remaining water masses as if they adhered to mass conservation in the ratio as before.

2.3. Satellite Observations and Reanalysis Data

Sea ice concentration (SIC): We use daily data from the High Latitude Level 3 Global AMSR SIC product that is provided by the Danish Meteorological Institute. It has a 10 km horizontal resolution derived from observations of the Advanced Microwave Scanning Radiometer 2 (AMSR-2) satellite (Lavelle et al., 2016).

Sea surface temperature (SST): We use daily data from the Group for High-Resolution Sea Surface Temperature (GHRSSST) Level 4 SST analysis that is provided by the Danish Meteorological Institute. It is derived from multiple satellites using an optimal interpolation approach on a global 0.05° grid (Høyer et al., 2014).

3. Results

3.1. Observations of a Subsurface Polar Water-Atlantic Water Front and a (Near-)Surface Polar Water-Surface Water Front

In the upper 5–30 m of Transect 1, we observe a strongly stratified, cold, and very fresh surface layer with minimum salinities of 32.6 psu (Figures 2a and 2c). This layer was likely generated by the melting of sea ice in the study area during the preceding weeks. The ice only receded about a week before this observation (Figure 1c). This water largely classifies as Surface Water (SW, Figure 2e) that occupies the upper 20 m of the transect

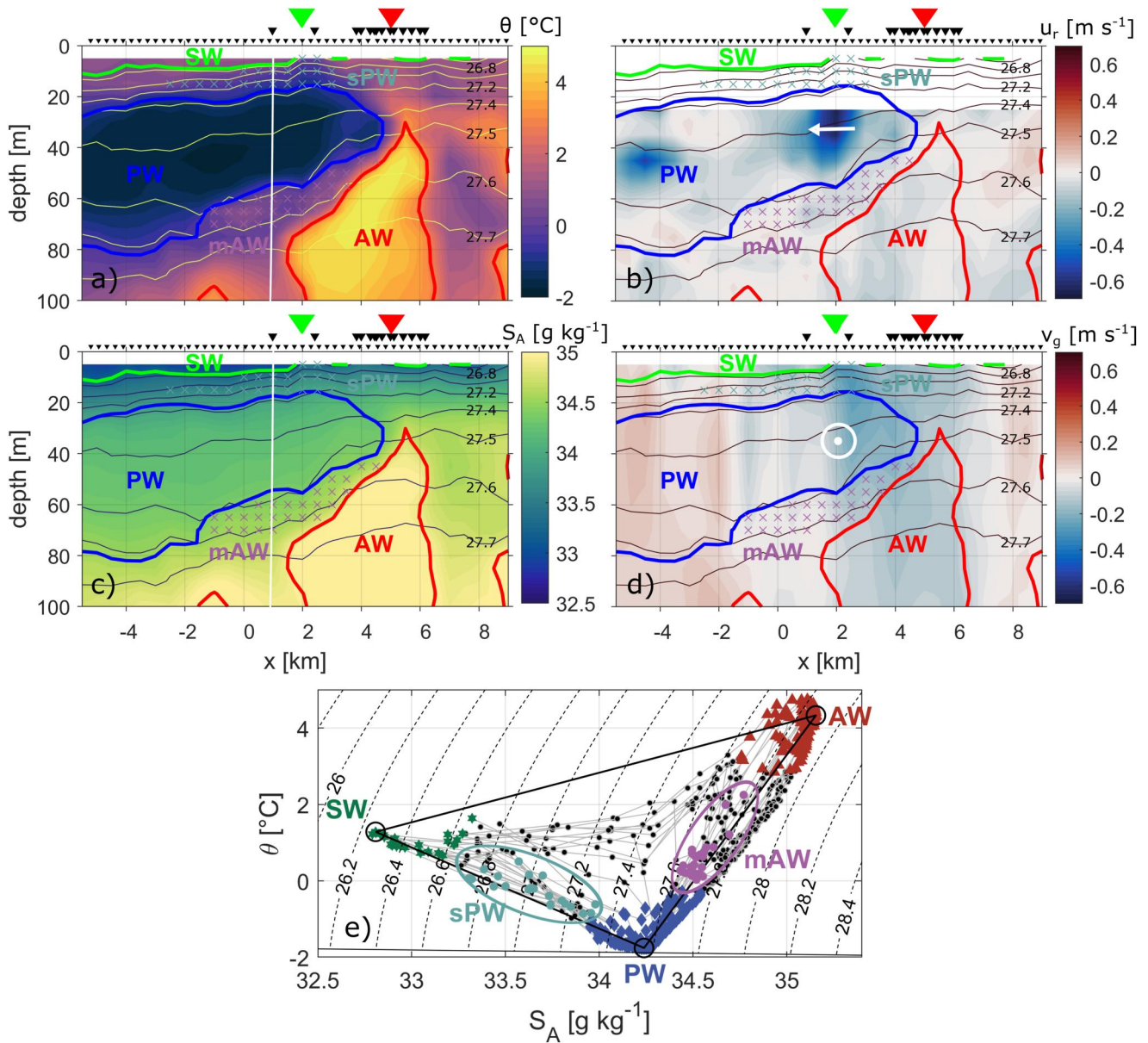


Figure 2. (a) Conservative temperature (θ) [$^{\circ}\text{C}$], (b) rotated along-transect velocity (u_r) [m s^{-1}] (negative to the left, i.e., southeastward, as indicated by the white arrow), (c) absolute salinity (S_A) [g kg^{-1}], (d) across-transect geostrophic velocity (v_g) [m s^{-1}] (negative out of the page, i.e., northeastward, as indicated by the white symbol). Also indicated are contours of potential density anomaly [kg m^{-3}] and 75% water mass fraction contour lines (red: Atlantic Water, AW; blue: Polar Water, PW; green: Surface Water, SW). Crosses denote (near-)surface Polar Water (sPW, cyan) and mixed Atlantic Water (mAW, magenta). Small black triangles on top indicate individual profiles and large black triangles indicate surface drifters that passed Transect 1 within the 36 hr before and after we conducted the transect. Large colored triangles indicate the (near-)surface front at 5 m depth (green) and the subsurface front at 30 m depth (red). The white line in panels (a, b) indicates a theoretical profile location further elaborated in Section 3.1. (e) θ - S_A diagram of Transect 1 with AW, PW, and SW definitions (black circles) and mixing lines (black). Individual profiles connect with a thin gray line. All measurements falling within $\geq 75\%$ of each water mass are colored as in panels (a–d).

(Figures 2a–2d). Below the SW layer, there is a well-mixed tongue of cold water near the freezing point in the southeastern half of the transect (Figure 2a), which classifies as PW (Figure 2e). At $x = 2$ –3 km, there is a significant PW fraction mixed into the SW, which we will refer to as “(near-)surface Polar Water” (sPW, cyan in Figure 2e). This sPW represents a 1 km wide sPW filament between relatively pure SW southeast and mixed AW and SW northwest of the filament, which results in two (near-)surface fronts. The southeastern horizontal buoyancy gradient amounts to $4 \times 10^{-6} \text{ s}^{-2}$ at 5 m depth. The northwestern horizontal buoyancy gradient of the opposite sign is shallower and weaker, and thus above the range covered by our observations, and we will not

discuss it further here. The southeastern (near-)surface front (large green triangle, Figures 2a–2d) is associated with northeastward geostrophic velocities of up to 0.6 m s^{-1} (negative along-transect velocities, Figure 2b, and negative in-situ across-transect velocities, Figure 2d). The sPW filament is an example of a salinity-stratified surface layer that is mixed to a varying degree with PW and AW below, yielding multiple shallow (near-)surface fronts that each have their associated geostrophic flows. The degree of mixing with either PW or AW may be related to the dynamics of the subsurface front as further discussed in Sections 4.1.2–4.1.4, though it may also be a mere coincidence that the (near-)surface and subsurface fronts are in close proximity.

The warmest and most saline water (i.e., the AW, with potential temperatures and salinities of up to 4.8°C and 35 psu, respectively, Figures 2a and 2c) resides directly below the PW in the southeastern half and much shallower below the SW in the northwestern half of the transect. We find that the highest AW fractions are within the largest filament in this transect. The AW filament is located between $x = 2\text{--}6.5 \text{ km}$, occupying the space underneath the PW toward the southeast and reaching up to 30 m below the SW in the northwest. Thus, below the surface layer, we observe a subsurface front with a buoyancy gradient of up to $7 \times 10^{-7} \text{ s}^{-2}$ at 55 m between the main bodies of PW and AW. This buoyancy gradient is about five times smaller than the one of the (near-)surface front but stretches over a depth range of 30–85 m. Between the PW and AW, we find a mix of PW and AW, with a small SW fraction, which we will refer to as “mixed Atlantic Water” (mAW, Figure 2e). The subsurface front (large red triangle, Figures 2a–2d) is also associated with a northeastward flow, albeit with weaker velocities than the (near-)surface front (Figures 2b and 2d). 15 out of 19 deployed surface drifters that did not leave the study region toward the southwest, pass Transect 1 less than 36 hr before or after the occupation of Transect 1 shown in Figure 2. Except for two drifters, they all cross the transect above the AW filament (large black triangles, Figures 2a–2d), moving northeastward with the geostrophic flow likely associated with the sharp front on the southeastern side of the filament. While the surface drifters are moved by the surface flow and the density gradient only appears subsurface, the baroclinic nature of the associated geostrophic flow means that the horizontal flow can only change to some extent across the less than 25 m thick stratified surface layer. We conclude that the subsurface front also affects the surface flow. We deployed the drifters equidistantly (2 km) along multiple earlier transects (Figure 4) so they clearly converge. We assume the convergence to be related to frontal dynamics, indicating downwelling as part of an ageostrophic circulation typically associated with submesoscale fronts. The measurements along Transect 1 do not cross the surface front between SW and AW, which was located further east of the transect. In the entire study region, we do not observe a mixed layer (stratification reached up to the shallowest observation at 5 m depth). However, we observe surface flow of the drifters associated with the subsurface front, suggesting that subsurface dynamics may influence or even cause spatial variability in the stratified (near-)surface layer, creating more shallow fronts.

At both the (near-)surface front between SW and sPW, and the subsurface front between PW and AW, we expect to see subduction of the denser water mass below the lighter water mass. We use the SW fraction as a tracer for the subduction of AW below PW. We know, the AW is situated at the sea surface in eastern Fram Strait. On its way westwards, it must subduct either below SW and PW, if SW is present, or directly below PW. As water subducts, the denser water mass mixes with the lighter one to a certain degree. That is why we see SW mixed into the AW from above, but not in the PW. A small SW fraction ($\sim 5\%$) is present between the PW and the AW, along the tilted isopycnals of the front (Figure 3a), which is thus an indicator that the AW (together with a small fraction of SW) is subducting below the PW. The water mass between the PW and AW ends up being mainly a mixture of the two, with the added small SW fraction (mAW, magenta crosses, Figure 2e). In the mAW along the subsurface front, the chlorophyll *a* concentration is enhanced up to $0.54 \mu\text{g L}^{-1}$ (magenta contour, Figure 3b), nitrate is depleted (Figure 3c), and oxygen is saturated (Figure 3d) compared to the surrounding water at the same depth. As the subsurface front is located largely below the euphotic depth (white contour, Figures 3b–3d), active growth cannot be an explanation, and this water must have subducted.

We cannot use SW as a tracer for subduction at the (near-)surface front, as, in this case, PW would subduct below SW and may simply mix with it in the process. The characteristics of the sPW filament are, however, also visible below the SW toward the southeast (cyan crosses, Figure 3), but this could also have been caused by turbulent mixing between the SW and the PW below. Below the SW in the southeast, there is a patch of high chlorophyll *a* concentration (cyan contour, Figure 3b) that is part of an enhanced band at 10–20 m depth present along the entire transect—this qualitatively agrees with light transmissivity, indicating that photochemical quenching cannot explain this pattern, as we are far from the sea floor and anything that influences light transmissivity is likely chlorophyll. This band could have been part of the spring bloom that propagated downwards, as nutrients depleted

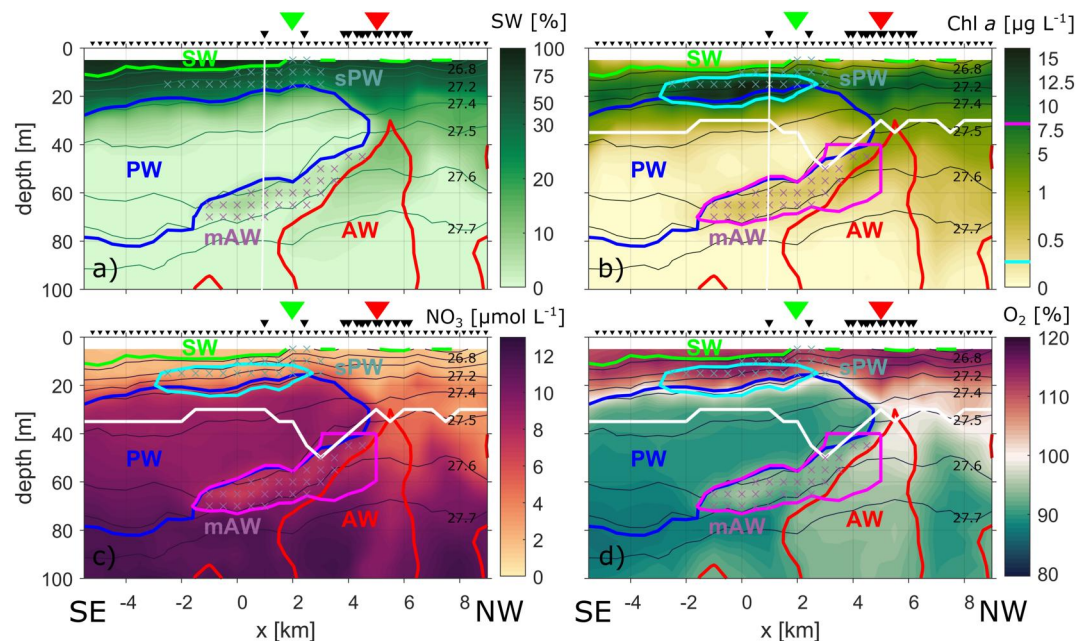


Figure 3. Same as Figure 2, but with (a) SW water mass fraction [%], (b) chlorophyll *a* (*chl a*) fluorescence [$\mu\text{g L}^{-1}$], (c) nitrate (NO_3) concentration [$\mu\text{mol L}^{-1}$], and (d) oxygen (O_2) saturation [%]. Note the nonlinear color bars in panels (a, c). In panels (b–d) we also show the euphotic depth (white), $\geq 50\%$ of the subsurface maximum of chlorophyll *a* (below 50 m, $0.27 \mu\text{g L}^{-1}$, magenta contour), and $\geq 50\%$ of the overall maximum of chlorophyll *a* near the surface ($8.10 \mu\text{g L}^{-1}$, cyan contour).

at the surface. The patch below the SW southeast of the (near-)surface front showed increased values of chlorophyll *a* up to $16.2 \mu\text{g L}^{-1}$ and subduction of high-chlorophyll *a* water from the surface may have contributed to the formation of this particular patch. The water is depleted of nitrate above 20 m (Figure 3c), oversaturated with oxygen (Figure 3d), and the chlorophyll *a* patch is well within the euphotic depth (white contour, Figures 3b–3d), indicating favorable conditions for primary production.

Tracers such as water mass signatures, chlorophyll *a* concentration, nitrate, and oxygen saturation are useful for identifying subducted water masses, which may no longer have a velocity signal at the time of observation. Here, we observe the subsurface subduction of AW below a stratified surface layer and posit that some of this water must have initially subducted below the surface layer before our observations, as well as subduction potentially enhancing the concentration of a chlorophyll *a* patch at a (near-)surface front that resulted from spatial variability in said stratified surface layer.

3.2. Subsurface and (Near-)Surface Front as Part of a Mesoscale Atlantic Water Filament Separating Polar Water From the Marginal Ice Zone

In addition to Transect 1, we conducted four more transects with the Triaxus towed vehicle on the night of 14/15 July at the same along-track horizontal resolution. These transects allow us to add a 2-dimensional horizontal view to our analysis. The set of transects took 12 hr to complete and may thus contain some temporal variability on submesoscale time scales. Other observations, such as SST, wind, and SIC are only available hourly or daily. For this analysis, we focus on the spatial distribution of water masses and assume the observations were carried out fast enough to reflect spatial rather than temporal variability.

The SST distribution on 14 July (Figure 4a) shows a wedge of warmer water protruding toward the north in the western part of the map and colder water protruding toward the south in the central part of the map. The northwesterly 10 m wind pushed the nearby sea ice and associated fresh meltwater northwest of the transect back toward the study region. This may have contributed to meltwater further separating the AW filament from the sea surface, contributing to its subduction.

Our high-resolution observations reveal the submesoscale complexity of the subsurface AW filament extending into the PW (Figure 4b, boundaries of filament are shown by dashed and solid red contours). The filament consists

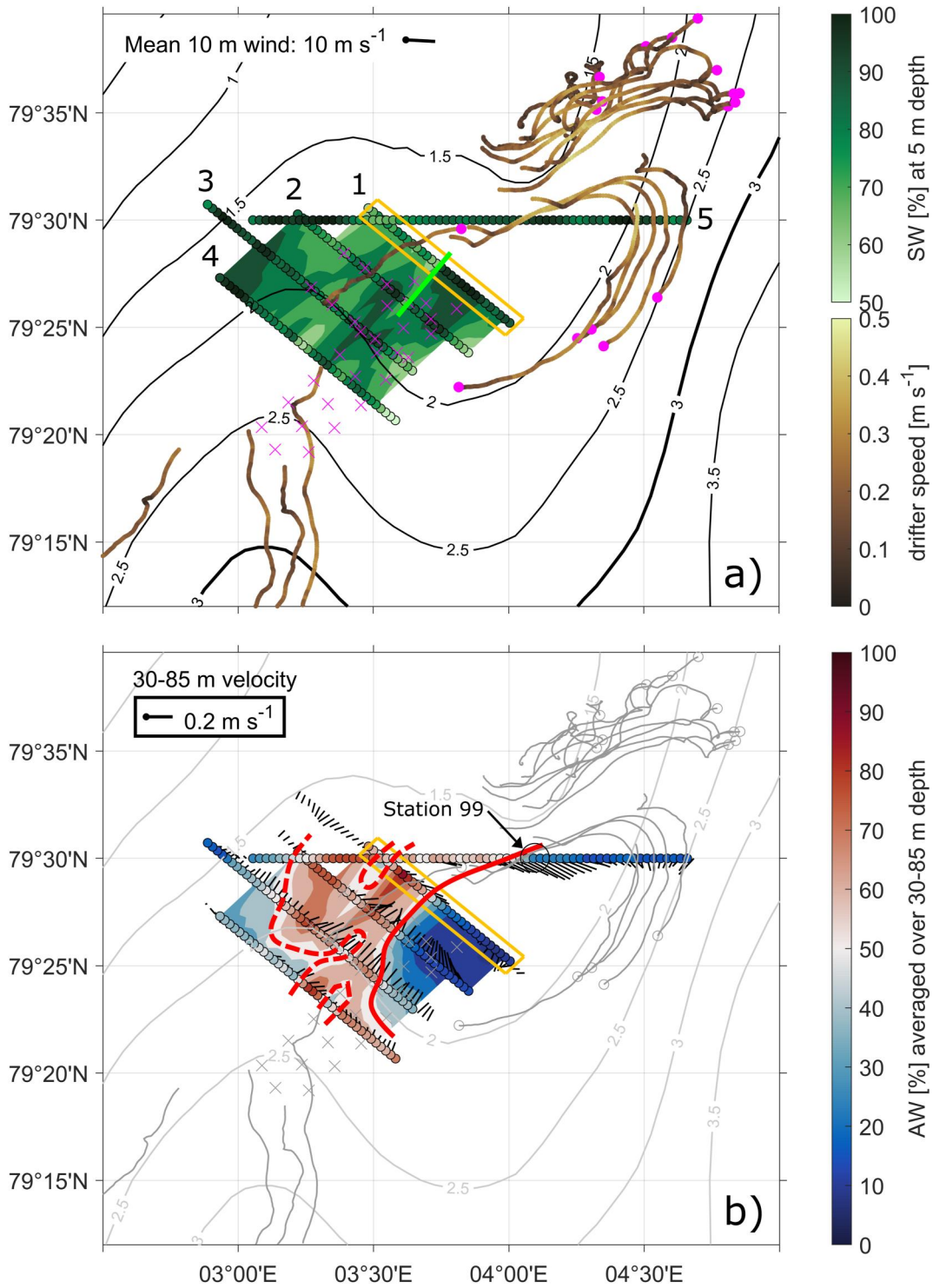


Figure 4.

of multiple limbs ranging in width between 2.5 and 5 km, with the one containing the highest AW fraction visible in Transect 1 as the main filament (~4 km wide). The subsurface front between PW and AW present in Transect 1 also extends across Transects 2, 3, and 5 (red solid contour) between the high fraction AW limb and the PW protrusion on the eastern side of our observations. Counterintuitively, in Transect 1, PW is present on the side of the transect further away from the sea ice, while AW resides on the side closer to the sea ice. Such a water mass distribution would be consistent with an AW protrusion as part of an eddy, separating PW from the sea ice. There is PW near the ice edge on the northwestern side of the AW filament, as captured in the measurements of Transects 3–5.

Most of the drifters still present within the study region move toward the northeast with speeds of up to $\sim 0.5 \text{ m s}^{-1}$ (magenta dots, Figure 4a). The remaining drifters are moving southeastwards, presumably with the geostrophic flow induced by the large-scale surface gradient (by 15 hr after the observations outside the study region in Figure 4a), with only one drifter still present near our transects, though it also moved toward the northeast. The larger portion of drifters thus moves along the subsurface front with the associated geostrophic flow directed northeastwards in the western part of the domain, steering eastwards in the eastern part (along the AW filament shape). The subsurface velocity measurements show a similar pattern (Figure 4b). At 5 m depth, instead, we observe the strong (near-)surface front between the SW above the PW tongue and the sPW filament with a lower fraction of SW (Figure 4a, green line) both in Transect 1 and 2, suggesting it to be a very local phenomenon (both in the horizontal and the vertical). Along this front, we also see a few drifters passing (Figure 2), though it is unclear whether this is due to frontal dynamics similar to the subsurface front. Eventually, some of the drifters are caught in the southward geostrophic flow of the surface front east of the observations (Figure 4a).

Overall, the shape of the AW filament resembles that of a mesoscale eddy, separating PW from the sea ice edge. It displays multiple submesoscale limbs that we could not have observed with lower-resolution measurements. The SW layer separates the filament from the surface, and subsurface fronts may affect surface motion, while shallow (near-)surface fronts within the surface layer may have their own velocity signal.

4. Discussion

4.1. Subduction Processes Along (Near-)Surface and Subsurface Fronts

Based on the detailed analysis of Transect 1 and its spatial context, we discuss the processes (shown in Figure 5) that may have caused the observed situation and their associated dynamics. The numbering of processes does not imply any temporal relation between the processes (i.e., process 1 has not necessarily occurred before process 2, and so on).

4.1.1. Subsurface Frontal Dynamics

- (1) *Convergence of SW and downwelling of mAW*: Previous studies have shown that on submesoscale length scales, convergence occurs at density fronts and can lead to the accumulation of surfactants like surface drifters (D'Asaro et al., 2018), plastics (Wang et al., 2022) or sea ice (von Appen et al., 2018). In our observations, surface drifters cross Transect 1 between $\sim x = 4\text{--}7 \text{ km}$ (Figures 2a–2d, and schematically in Figure 5, black rectangle) within 36 hr before and after the observations and with a horizontal separation along Transect 1 of a few meters to 300 m. This clustering indicates a convergence and downwelling, where surfactants like the surface drifters or mobile sea ice (von Appen et al., 2018), but also lighter water masses like the SW accumulate along the front (Figure 5). The subsurface front is associated with (a-)geostrophic motion that, due to its baroclinicity, is likely also impacting the surface, despite the presence of

Figure 4. (a) Fraction of Surface Water (SW) [%] at 5 m depth from interpolated observations of Transects 1–5 on 14 July 15:29–15 July 03:36 UTC (indicated by the black circles). The (near-)surface front analyzed in Section 3.1 is marked with a solid green line. Black contour lines display sea surface temperature (SST) [°C], the black line directed away from the dot 10 m wind [m s^{-1}], averaged over the time, the transects were conducted. Also shown are the surface drifter locations 15 hr after the end of the measurements shown here (magenta dots), their location of deployment (magenta crosses), and their trajectory during the 15 hr before and after the transects were conducted, as well as their speed [m s^{-1}]. (b) Fraction of Atlantic Water (AW) [%] averaged over 30–85 m depth from observations during the same time. The subsurface front analyzed in Section 3.1 is marked with a solid red line and other fronts that were part of the AW filament with a dashed red line, marking the 50% AW fraction. Black lines indicate the velocities averaged over the same depth [m s^{-1}]. SST [°C] and drifter tracks from (a) are gray. A larger black circle indicates the location of station 99 shown in Figure 6. In both panels, an orange rectangle marks the location of Transect 1.

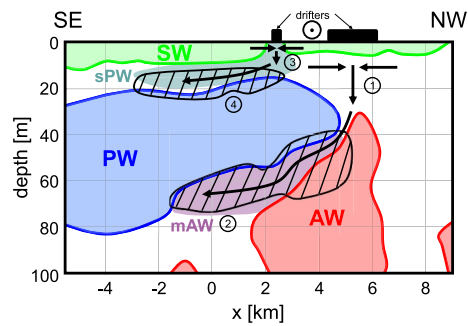


Figure 5. Schematics of water mass distribution and frontal dynamics related to the subsurface front between lighter Polar Water (PW) and denser Atlantic Water (AW), and the (near-)surface front between lighter Surface Water (SW) and denser (near-)surface PW (sPW). The areas in which the water mass fractions exceed 75% are shown in green (SW), blue (PW), and red (AW). The processes discussed in the text are (1) convergence of SW and downwelling of mAW, (2) subsurface subduction, (3) convergence and downwelling of sPW, and (4) near-surface subduction. Hatched areas show the subduction areas derived from 50% of the near-surface and subsurface maximum chlorophyll *a* fluorescence. We schematically extrapolate outside the range of our measurements (above 5 m depth).

a shallow stratified surface layer above the subsurface front. This means not only a surface mixed layer front can induce convergence and geostrophic motion at the sea surface. Hence, a subsurface front may influence the distribution of surfactants and SW.

- (2) *Subsurface subduction:* Previous subduction of mAW may be inferred from the subsurface presence of a non-negligible fraction of SW (Figure 3a) and the maximum in chlorophyll *a* fluorescence below the euphotic depth (Figure 3b, and schematically in Figure 5, subsurface hatched area). Koenig et al. (2020) also observed a subsurface front between AW and modified AW from the Arctic Ocean, collocated with a surface front between AW and what we would categorize as SW. Both the depths of the fronts and the associated maxima in chlorophyll *a* fluorescence are very similar to our observations, although Koenig et al. (2020) observed the presence of a mixed layer on both sides of the front. The study by Koenig et al. (2020) highlights that such collocation of frontal features and vertical displacement of biogeochemical properties as we observe them are not uncommon, which strengthens the claims that meltwater can accumulate above a subsurface front due to convergence and downwelling (process 1) and that biogeochemical properties can subduct along subsurface fronts (process 2).

4.1.2. (Near-)Surface Frontal Dynamics

- (3) *Convergence and downwelling of sPW:* Multiple drifters pass transects 1 and 2 close to the (near-)surface front ($\sim x = 2.5$ km, schematically in Figure 5, black rectangle) within 36 hr before and after the observations. One explanation for this could be the proximity of the (near-)surface and subsurface fronts, and these drifters are also associated with the convergence above the subsurface front (process 1). Alternatively, the (near-)surface front itself could have caused convergence and downwelling of sPW (as illustrated in Figure 5). Such dynamics are only possible when a mixed layer is absent. As the sPW filament is much more localized than the AW filament (both horizontally and vertically, albeit with a stronger horizontal buoyancy gradient), this convergence may have affected fewer drifters. We deployed drifters with a horizontal spacing of ~ 2 – 3 km (more than submesoscale length scales in the Arctic) only 4 and 1.5 days before the realization of Transect 1. That leaves some chance as to which nearby front they were deployed the closest to and are thus the most likely to converge along. In bigger drifter studies (i.e., more drifters, higher horizontal resolution, temporal/spatial coverage), the most prominent front likely affects the drifters most (e.g., D'Asaro et al., 2018). The potential convergence along the (near-)surface front is above a strong northwestward velocity signal between 25 and 50 m depth. Regardless of whether this velocity signal is related to the (near-)surface or the subsurface front further to the northwest, it indicates active frontal dynamics (such as a geostrophic current).
- (4) *Near-surface subduction:* One explanation for the strong near-surface chlorophyll *a* fluorescence maximum (Figure 3b, schematically in Figure 5, hatched (near-)surface area) is subduction of the (denser) sPW below the (lighter) SW. This subduction would agree with the initial downwelling of sPW from the surface (as argued in the previous paragraph) and may thus have removed water high in chlorophyll *a* from the surface. By such means, the spatial variability of the SW layer would contribute to chlorophyll *a* patchiness. The subduction is not necessarily related to the observed (near-)surface front here, as the front was so localized.

Another explanation is that the chlorophyll *a* maximum is caused by localized primary production at the nitracline in a strongly stratified environment. A very similar patch of chlorophyll *a*, in terms of depth, location, vertical extension, and magnitude, was observed in Fram Strait in 2016 by Tippenhauer et al. (2021). They concluded that the chlorophyll *a* grew locally but was sustained by vertical nutrient fluxes related to submesoscale dynamics. In the Nansen Basin near the ice edge, Koenig et al. (2020) observed a weaker and slightly deeper (down to 40 m) subduction of chlorophyll *a* below colder and fresher surface water from a surface maximum in the AW mixed layer. In Fram Strait, Wulff et al. (2016) found that phytoplankton accumulated at a front (due to downwelling as part of an ageostrophic secondary circulation, ASC) and then subducted. These studies show that submesoscale dynamics affect the vertical export of phytoplankton both by actively moving it vertically and enhancing its

production locally. One needs to note, however, that the physical setting we observe is distinct from that of the abovementioned studies in one aspect. We study a stratified surface layer in contrast to the pronounced mixed layers in the other three studies, where the nutrient-poor SW layer forces the chlorophyll *a* maximum to migrate downwards. (Near-)surface fronts in this stratified surface layer likely impact biological parameters by providing an additional mechanism of subduction.

4.1.3. Relationship of Subsurface and (Near-)Surface Frontal Dynamics

We observe and imply different processes here. First, the process we are most confident about is process 2, subsurface subduction, which we know has happened by observing significant amounts of chlorophyll *a* along a subsurface front between PW and AW, below the euphotic depth. The subsurface presence of AW mixed with SW implies earlier subduction of surface AW from a mixed layer below the stratified SW layer. Second, the subsurface front may influence the SW distribution by accumulating SW above (process 1, convergence of SW and downwelling of mAW) and creating meltwater fronts such as the (near-)surface front between sPW and SW observed here. It is possible, though, that the collocation of the subsurface and (near-)surface front is a mere coincidence. Additionally, the wind has a large effect on SW distribution. Third, the (near-)surface front displays signs of active frontal dynamics, such as the strong velocity signal and the potential drifter accumulation (process 3, convergence and downwelling of sPW), and the (near-)surface chlorophyll *a* patch that may have subducted (process 4, near-surface subduction). It is possible, though, that the velocity signal and the drifter accumulation are related to the subsurface front, and/or that the near-surface chlorophyll *a* patch was locally produced. Last, this leads us to further elaborate process 2 and the proposal of the concept of "stepwise subduction."

4.1.4. Stepwise Subduction

The presence of SW in the subducted water in our transect suggests the following: the subducting water mass is mainly AW, but it also entrained some of the SW, likely when the two water masses met at the surface, where there was an AW mixed layer present (probably east of our study region, further away from the ice). Then, the lighter SW forced the much denser AW-SW mixture to subduct. When the AW-SW mixture subsequently met the comparably lighter PW below the SW layer, it had to subduct again, while it entrained PW and thus formed the mAW (process 2 in Figure 5). This suggests a stepwise subduction history along vertical staircases, with weaker horizontal density gradients and vertical stratification as the depth increases. With each subduction "step," properties of the lighter water mass are entrained into the subducting water mass, making each water layer more horizontally uniform (i.e., weaker gradients). This process may be intermittent in time and space. Here, we interpret two fronts to represent the two different steps in time and depth (though nearby horizontally). However, we do not see these two fronts as part of the same "staircase" as their formation was likely separated in time. The first step of a staircase can be one of the following three: (a) the surface front between the mixed layers of PW and AW, (b) the surface front between stratified SW and the mixed layer of AW, or (c) shallow fronts between the spatially intermittent SW and denser water. Our interpretation of the data is that we only observed the third type, which we refer to as (near-)surface front (green triangle in Figures 2a–2d and 3, green line in Figure 4a). Subsequent steps can be one of the following two: (a) subsurface fronts between PW and AW as presented in this study (red triangle in Figures 2a–2d and 3, red solid line in Figure 4a), or (b) horizontal density gradients between AW modified to varying degrees.

Mixed layer fronts (here between an AW mixed layer and a PW mixed layer as a first subduction step) are created as follows: atmospheric forcing or mesoscale straining generate lateral buoyancy gradients, which slump due to gravitational instability. Variability in initial stratification and forcing creates lateral density gradients (i.e., fronts) that are soon affected by rotation and as thermal wind balance is established, the slumping comes to a halt. To disturb the thermal wind balance, ageostrophic baroclinic instabilities act to further re-stratify the surface ocean (Boccaletti et al., 2007; Haine & Marshall, 1998). Baroclinic instability (in this case the same as mixed-layer instability) extracts available potential energy (APE) from the lateral density gradient as a function of the mixed layer depth, which produces larger vertical velocities compared to, for example, mesoscale-driven surface frontogenesis (Callies et al., 2015). APE is converted into eddy kinetic energy (EKE) and thus energizes the submesoscale and mesoscale eddy field, constituting a backward energy cascade (Callies et al., 2015).

A surface front between a mixed layer and a stratified surface layer (here between an AW mixed layer and a stratified SW layer, also as a first subduction step), on the other hand, does not necessarily derive from

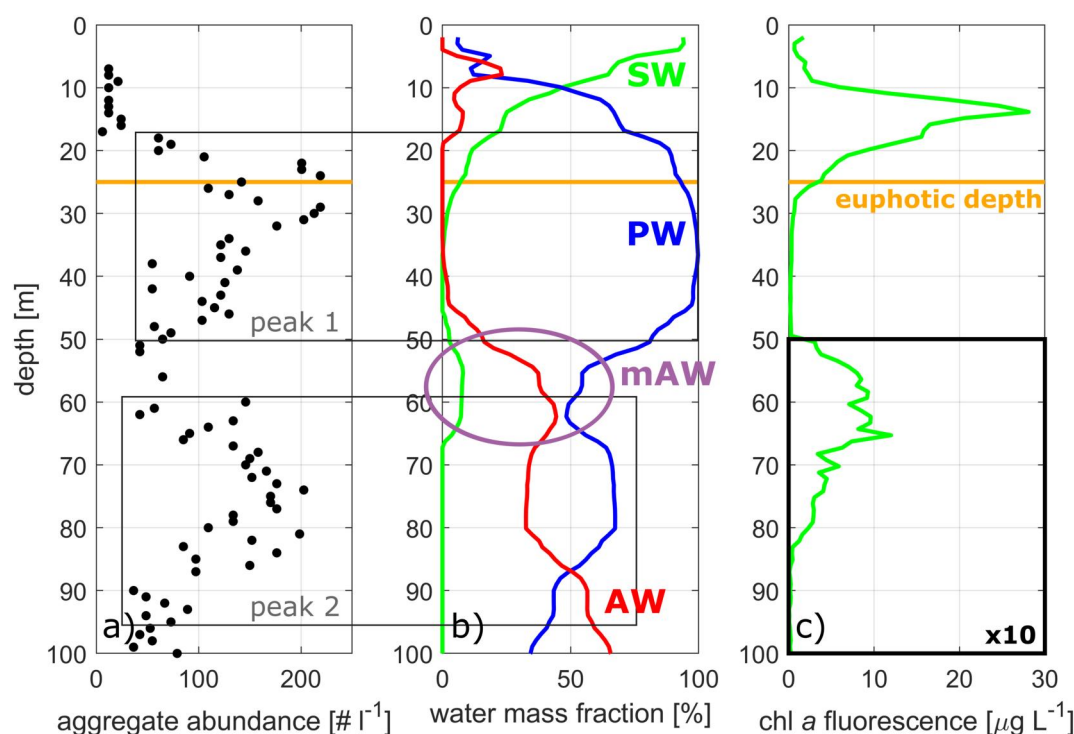


Figure 6. Vertical profiles at station 99 along Transect 5 of (a) aggregate abundance [$\# l^{-1}$], (b) water mass fractions [%] of Surface Water (SW, green), Polar Water (PW, blue), and Atlantic Water (AW, red), and (c) chl *a* fluorescence [$\mu g L^{-1}$]. Note that chl *a* fluorescence is multiplied by 10 between 50 and 100 m depth to enhance the visibility of the lower peak (black rectangle). Gray rectangles mark aggregate abundance peaks (peak 1, 2). A magenta circle highlights mixed AW (mAW). The orange line indicates the euphotic depth.

atmospheric forcing or mesoscale straining ultimately leading to baroclinic instability but may draw energy from the frontal circulation itself (D'Asaro et al., 2011). Due to the vertical shear of the frontal jet, the strong lateral density gradient, and weak stratification of the front, PV can become negative, indicating that fluid is not exchanged just vertically, but also along slantwise paths in symmetric instability (Haine & Marshall, 1998). Symmetric instability extracts mean kinetic energy from the geostrophic flow (opposite to baroclinic instability) and transfers the energy to smaller scales, where it is dissipated, constituting a forward energy cascade, depending on whether symmetric or baroclinic instability dominates (Thomas et al., 2013). Furthermore, symmetric instability can be sustained by down-front winds or destabilizing convection, which would favor a forward energy cascade. Increased turbulence, which may have been caused by forced symmetric instability, was observed along a front, which we would categorize as between an AW mixed layer and a stratified SW layer by Koenig et al. (2020) in the Nansen Basin of the Arctic Ocean.

A subsurface front below a stratified surface layer as we observe it here between PW and AW and assume as a second subduction step, on the other hand, gains its energy solely from a lateral density gradient without the deep mixed layer. It seems likely that it would also extract energy from the geostrophic flow and transfer kinetic energy to smaller scales, cascading energy forward through symmetric instability. As baroclinic instability may prove much less effective outside the mixed layer, this could be an efficient way of enhancing dissipation at smaller scales. However, in the subsurface, symmetric instability cannot be sustained by wind or destabilizing convection and may be rather transient, and much harder to observe.

4.1.5. Impact on Biology

We consider aggregate abundance observations to further corroborate the concept of stepwise subduction. We observe peaks in aggregate abundance at multiple stations. Shown here is station 99 (Figure 6a, for location see Figure 1c). The station is not located on Transect 1, but on transect 5, as we have no available aggregate abundance measurements on Transect 1. The upper peak (peak 1, its vertical extent marked by the upper gray box)

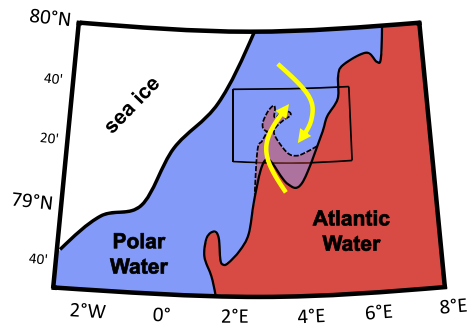


Figure 7. Schematic of Atlantic Water (AW) (red), Polar Water (blue), and sea ice (white) distribution on 13 July 2020. Surface properties are derived from the 20% sea ice and the 3°C sea surface temperature contour (solid black line, opaque filling). Subsurface properties (below the Surface Water) are derived from the 50% AW mass fraction contour (dashed black line, transparent filling) from our observations. The black rectangle indicates our study region. Yellow arrows indicate the general motion of the entire feature, derived from water mass distribution and surface drifter motion.

is between 18 and 50 m depth, where PW dominates (Figure 6b), just below the maximum in chlorophyll *a* concentration at 14 m ($28.1 \mu\text{g L}^{-1}$, Figure 6c). The lower peak (peak 2, its vertical extent marked by the lower gray box) is between 59 and 95 m, where the water was a mixture of PW and AW, mainly below the secondary maximum in chlorophyll *a* concentration at 65 m ($1.2 \mu\text{g L}^{-1}$, Figure 6c), substantially below where sufficient light for primary production would be available (see Figure 6 for euphotic depth, orange line). The secondary maximum in chlorophyll *a* concentration is within the mAW (small fraction of SW, Figure 6b).

The water mass distribution and chlorophyll *a* maxima are very similar to Transect 1, even though the station is located ~ 8 km northeast of the transect and was conducted 19 hr later. Station 99 is located along the same subsurface front between PW and AW that we observe in Transect 1 (red line in Figure 4), slightly more on the PW side. Vertically, transect 5 (not shown) displays the same signatures of subsiding mAW and chlorophyll *a* below PW in the west. We presume that a camera profile at the corresponding location in Transect 1 (near the subsurface front, slightly on the PW side, indicated by the white line, Figures 2a, 2c, and 3a) would yield a similar aggregate abundance profile.

Both particle abundance maxima are 10–15 m below the corresponding chlorophyll *a* maximum, which suggests that the particle maxima are material, either single phytoplankton cells or aggregates, that subsided from the (near-)surface in a single step (peak 1) or a second step (peak 2). The stepwise subsidence would thus lead to a downward shift of particle transport and aggregate formation, which could enhance POC export out of the upper mixed layer. Since the deeper water column is more homogenous in temperature and salinity, settling aggregates are exported more efficiently compared to the export in near-surface waters where aggregates can be retained by vertical density gradients (Alldredge et al., 2002; MacIntyre et al., 1995). Hence, transport via subsidence may provide a mechanism whereby particles and aggregates can leave the surface ocean faster. They may thus be less subjected to microbial degradation (Giering et al., 2014) or zooplankton feeding (Iversen et al., 2010), which would increase the efficiency of the biological carbon pump.

Generally, the conditions in which we carried out our measurements fall into what von Appen, Waite, et al. (2021) dubbed the “meltwater regime” where the upper tens of meters are highly stratified. Toward the east in Fram Strait, we would expect a surface front between lighter PW or SW and denser AW, where initial subsidence of AW from the mixed layer is much more efficient than from more localized (near-)surface gradients in a stratified surface layer. In the “meltwater regime” von Appen, Waite, et al. (2021) found phytoplankton blooms to be vertically constrained and of longer duration, as they were retained longer in the upper water column. A stepwise subsidence process may counteract this vertical constraint by increasing vertical export below the stratified surface layer via multiple steps. In 2020, the “meltwater regime” dominated Fram Strait (see von Appen, Waite, et al. (2021), their Figure 2a). In the “mixed-layer regime,” on the other hand, von Appen, Waite, et al. (2021) found the blooms were more intense and short-lived, and biological material was more readily exported through sinking toward the seafloor. As vertical motion induced by mixed layer fronts reaches deeper than the subsidence of AW below a meltwater layer, submesoscale fronts in the “mixed layer regime” would presumably export carbon more efficiently than stepwise subsidence, where individual steps may be intermittent in time and space. Hence, the carbon pump is still most efficient in the “mixed layer regime,” but stepwise subsidence may contribute to making vertical export more efficient in the “meltwater regime.”

4.2. (Sub-)Mesoscale Variability Near the Marginal Ice Zone

We assume that the surface front between the stratified Surface Water (SW) or the PW mixed layer and the AW mixed layer was located in the eastern part of our study region, further away from the ice edge than the subsurface front. This constellation could happen when the MIZ widens and narrows during the melt season or when there is detachment of eddies trapping sea ice in their core and moving it above warmer water, which additionally increases ice melt (Manucharyan & Thompson, 2017). We observe a water mass distribution, where subsurface AW is found to the west of PW, even though the large-scale gradient is such that AW resides in the eastern part of Fram

Strait and PW in the western part. That seems to be compatible with an anticyclonic mesoscale feature, where AW protrudes in an eddying motion to the north(-east) and PW to the south(-west) (schematically shown in Figure 7), superimposed on the large-scale east-to-west gradient of AW to PW. The large-scale gradient is part of the global buoyancy forcing (e.g., Mauritzen, 1996) from which submesoscale processes (e.g., fronts) can gain energy without exhausting it (i.e., if a horizontally mixed state with zero gradients was achieved). This consistent large-scale gradient maintains (sub-)mesoscale flows across seasons and makes Fram Strait one of the regions that are special compared to the general open ocean, showing that submesoscale, mesoscale, and larger scales act in tandem to produce smaller scale patterns within larger scale patterns (e.g., Thomas et al., 2008).

Based on available SST and SIC satellite observations, the mesoscale feature that relates to our observations persisted for 9 days (8 days before and one day after the occupation of Transect 1), while the MIZ was relatively narrow, straight, and oriented from southwest to northeast. Another similar feature further south disappeared five days before "our" feature developed and lasted 11 days. These life cycles are consistent with mesoscale time scales.

The kinematics of the northward protruding AW on the western side and the southward protruding SW or PW on the eastern side resemble that of a mesoscale anti-cyclonic eddy with a diameter of ~30–50 km (arrows in Figure 7, similar to what e.g., Wekerle et al. (2020) found in the region) and PW in its center. From our high-resolution measurements, we can discern mesoscale and submesoscale filament extensions of this eddy pattern that manifest in the water mass distribution, subsurface velocities, and the motion of the surface drifters. The northward protrusion of AW extends in the subsurface along a filament that reaches a maximum width of 10 km and is at least 20 km long (mesoscale length scales) but splits up into multiple limbs that are between 2.5 and 5 km wide (submesoscale length scales, Figure 4b, schematically in Figure 7). Kozlov and Atadzhanova (2022) and Bashmachnikov et al. (2020) found that submesoscale and small mesoscale eddies dominate the eddy field in the Fram Strait MIZ, though they may deal with a detection bias, as smaller eddies are easier to identify in synthetic aperture radar data and open-ocean eddies are likely more difficult to detect in winter, when typically, more eddies are created. Both the literature and the present study suggest that there are submesoscale features within mesoscale features in the MIZ, even though they are typically not resolved in observations or models.

While high-resolution observational studies such as this one may contribute significantly to our understanding of submesoscale processes, they have exclusively been conducted in summer, yet the number and strength of eddies present in Fram Strait varies seasonally. EKE in the WSC is maximal in winter and advected westwards, peaking in central Fram Strait in spring (von Appen et al., 2016). Bashmachnikov et al. (2020) observed higher EKE and faster eddies in Fram Strait during winter. They also presented model results suggesting more small eddies in spring-early summer (when our study took place). Biddle and Swart (2020) found that submesoscale flows were most intense in the mid-winter in the Antarctic MIZ, mainly due to mixed layer instabilities. The depth to which we observe subduction in summer is likely a lower-bound estimate for the annual mean conditions. We expect the first subduction step from the AW surface mixed layer to export water vertically much more efficiently in winter. Further subduction steps may become increasingly independent from seasonal variability as they are removed from influences by the atmosphere.

In an Atlantifying and warming Arctic Ocean, the MIZ widens in summer (Strong & Rigor, 2013), and the transition of sea ice to open ocean recedes away from the Arctic Ocean boundaries. Hence, the processes discussed here will become more relevant. Large areas of this open ocean may be strongly meltwater stratified at the surface.

5. Conclusions

From the results of this high-resolution study of a submesoscale frontal system in the MIZ, we draw several conclusions. Before the cruise, we expected to find a surface front between AW and PW with outcropping isopycnals at the surface and water subducting from a well-defined mixed layer. In other parts of the ocean, subduction from the mixed layer has commonly been reported from observational studies (e.g., Archer et al., 2020; von Appen et al., 2020) and discussed in theory (e.g., Freilich & Mahadevan, 2021; McWilliams, 2021). We found, however, that near the ice edge summer ice melt can lead to very high near-surface stratification, with PW and AW residing below. The stratification can reach the surface, and there may not be a mixed layer.

Near the ice edge, we observe a subsurface front between PW and AW (mixed with a small fraction of SW) between 30 and 85 m depth. This front is associated with the subduction of water masses and biogeochemical properties. The AW must have been in contact with the atmosphere at some point and thus must have subducted below the SW in a first "step" and then below the PW in a second "step." We term this concept "stepwise subduction," where the subduction of water masses in the MIZ may originate at the surface but then iterates through fronts at multiple depths intermittently in time. Subsurface fronts may contribute to patchiness of the SW layer by convergence and downwards flow. We observe strong horizontal density gradients between the intermittent SW layer and (near-)surface PW (sPW) that only extend to 20 m depth, where the sPW potentially subducted below the SW. Subduction along a meltwater front may be an additional mechanism by which water subducts as a first "step."

The subduction from a deep mixed layer, for example, in the winter in Fram Strait, likely creates higher vertical velocities than a shallow meltwater front or a subsurface PW-AW front, as the horizontal density gradients are potentially stronger and reach deeper, and thus provide more APE. But as the subduction process iterates through multiple "steps," the transported material can reach greater depths compared to a single subduction "step," enhancing the carbon export. Subsurface fronts may be more prone to symmetric instability compared to mixed layer fronts that are subject to baroclinic instabilities. Subsurface fronts may thus cascade energy forwards rather than backward and contribute to increased dissipation, though symmetric instability may be rather transient.

The submesoscale features observed here are part of a larger mesoscale pattern in the SST gradient and the sea ice distribution in Fram Strait. We assume that most of the mesoscale fronts, meanders, filaments, and eddies that are commonly observed in the MIZ (e.g., Kozlov & Atadzhanova, 2022) are also associated with smaller submesoscale features. Occurrence of stepwise subduction requires a region, where we would expect strong lateral density gradients in the surface ocean, and a stratified surface layer. Strong lateral density gradients are typical in confluent regions near separating boundary currents, like the Gulf Stream (e.g., Thomas et al., 2013) and the Kuroshio Current (e.g., D'Asaro et al., 2011), along mid-oceanic water mass fronts, like the AW-PW front in Fram Strait (e.g., Hattermann et al., 2016) or the Barents Sea (e.g., Oziel et al., 2016) and the Almeria-Orian front in the Mediterranean Sea (e.g., Mahadevan et al., 2020), and in eddy-rich regions, like the Antarctic Circumpolar Current (e.g., Swart et al., 2020). Particularly the polar regions would be affected by sea ice melt in summer, with meltwater providing a stratified surface layer. In other regions, river runoff or net precipitation may contribute to near-surface stratification.

Submesoscale features are typically too small to be observed with satellites or modeled with climate models, and they are time- and work-intensive to observe thoroughly during ship campaigns. It is important to synthesize the large-scale, low-resolution data from satellites and models with the regional-scale, high-resolution data from ship campaigns, drifting platforms, and numerical simulations with appropriately high resolution. Future work should focus on a better process understanding, quantifying the overall effect of the submesoscale in different seasons and under receding sea ice cover, to consider it in (regional) numerical ocean models and coupled global climate models.

Data Availability Statement

The following data are available in PANGAEA: processed VMADCP (Hofmann, von Appen, & Mathieu, 2022), processed Triaxus (Hofmann, von Appen, Mathieu, et al., 2022), surface drifters (von Appen, Hoppmann, & Kuhlmeier, 2021), and shipboard CTD (Hoppmann et al., 2022). Sea ice concentration data are available in the EUMETSAT SAF on Ocean and Sea Ice (OSI-SAF, 2017). Sea surface temperature data are available in the Physical Oceanography Distributed Active Archive Center (Danish Meteorological Institute - Center for Ocean and Ice, 2007).

References

- Allredge, A. L., Cowles, T. J., MacIntyre, S., Rines, J. E. B., Donaghay, P. L., Greenlaw, C. F., et al. (2002). Occurrence and mechanisms of formation of a dramatic thin layer of marine snow in a shallow Pacific fjord. *Marine Ecology Progress Series*, 233, 1–12. <https://doi.org/10.3354/meps233001>
- Aravind, H. M., Verma, V., Sarkar, S., Freilich, M. A., Mahadevan, A., Haley, P. J., et al. (2023). Lagrangian surface signatures reveal upper-ocean vertical displacement conduits near oceanic density fronts. *Ocean Modelling*, 181, 102136. <https://doi.org/10.1016/j.ocemod.2022.102136>

Acknowledgments

Ship time for this study was provided under Grant GPF 18-1_33. The efforts of the captain and crew of RV *Maria S. Merian* are greatly appreciated, especially under the unique circumstances early in the pandemic. Special thanks also go to Laura Mathieu, Carina Engicht, David Kuhlmeier, Christian Konrad, and Simon Ramondenc for the work at sea they contributed. The authors gratefully acknowledge the funding by the Deutsche Forschungsgemeinschaft (DFG, German Research Foundation)—Projektnummer 268020496—TRR 172, within the Transregional Collaborative Research Center "Arctic Amplification: Climate Relevant Atmospheric and Surface Processes, and Feedback Mechanisms (AC³)." This study was supported by the DFG-Research Center/Cluster of Excellence "The Ocean Floor—Earth's Uncharted Interface" at MARUM, Research Unit Receiver and the European Union's Horizon 2020 research and innovation programme through the project Arctic PASSION under Grant agreement number 101003472. The authors thank the editor and the two reviewers for their constructive comments that have helped clarify a number of aspects in the study. Open Access funding enabled and organized by Projekt DEAL.

- Archer, M., Schaeffer, A., Keating, S., Roughan, M., Holmes, R., & Siegelman, L. (2020). Observations of submesoscale variability and frontal subduction within the mesoscale eddy field of the Tasman Sea. *Journal of Physical Oceanography*, 50(5), 1509–1529. <https://doi.org/10.1175/JPO-D-19-0131.1>
- Arrigo, K. R., Perovich, D. K., Pickart, R. S., Brown, Z. W., van Dijken, G. L., Lowry, K. E., et al. (2012). Massive phytoplankton blooms under Arctic sea ice. *Science*, 336(6087), 1408. <https://doi.org/10.1126/science.1215065>
- Bashmachnikov, I. L., Kozlov, I. E., Petrenko, L. A., Glok, N. I., & Wekerle, C. (2020). Eddies in the North Greenland Sea and Fram Strait from satellite altimetry, SAR and high-resolution model data. *Journal of Geophysical Research: Oceans*, 125(7). <https://doi.org/10.1029/2019JC015832>
- Beszczynska-Möller, A., Fahrback, E., Schauer, U., & Hansen, E. (2012). Variability in Atlantic water temperature and transport at the entrance to the Arctic Ocean, 1997–2010. *ICES Journal of Marine Science*, 69(5), 852–863. <https://doi.org/10.1093/icesjms/fss056>
- Biddle, L. C., & Swart, S. (2020). The observed seasonal cycle of submesoscale processes in the Antarctic marginal ice zone. *Journal of Geophysical Research: Oceans*, 125(6). <https://doi.org/10.1029/2019JC015587>
- Boccaletti, G., Ferrari, R., & Fox-Kemper, B. (2007). Mixed layer instabilities and restratification. *Journal of Physical Oceanography*, 37, 2228–2250. <https://doi.org/10.1175/JPO3101.1>
- Bodner, A. S., Fox-Kemper, B., Johnson, L., van Roekel, L. P., McWilliams, J. C., Sullivan, P. P., et al. (2023). Modifying the mixed layer eddy parameterization to include frontogenesis arrest by boundary layer turbulence. *Journal of Physical Oceanography*, 53(1), 323–339. <https://doi.org/10.1175/JPO-D-21-0297.1>
- Brenner, S. D., Rainville, L., Thomson, J., & Lee, C. (2020). The evolution of a shallow front in the Arctic marginal ice zone. *Elementa*, 8(1). <https://doi.org/10.1525/ELEMENTA.413>
- Callies, J., Flierl, G., Ferrari, R., & Fox-Kemper, B. (2015). The role of mixed-layer instabilities in submesoscale turbulence. *Journal of Fluid Mechanics*, 788, 5–41. <https://doi.org/10.1017/jfm.2015.700>
- Cornejo, P., & Bahamonde, A. (2023). Energy and information fluxes at upper ocean density fronts. *Fluids*, 8(17), 17. <https://doi.org/10.3390/fluids8010017>
- Danish Meteorological Institute - Center for Ocean and Ice. (2007). GHRSSST level 4 DMI-OI global foundation Sea Surface temperature analysis (GDS version 2) [Dataset]. *PO.DAAC*. <https://doi.org/10.5067/GHGD-4FD02>
- D'Asaro, E. A., Lee, C., Rainville, L., Harcourt, R., & Thomas, L. N. (2011). Enhanced turbulence and energy dissipation at ocean fronts. *Science*, 332(6027), 318–322. <https://doi.org/10.1126/science.1201515>
- D'Asaro, E. A., Shcherbina, A. Y., Klymak, J. M., Molemaker, J., Novelli, G., Gigand, C. M., et al. (2018). Ocean convergence and the dispersion of flotsam. *Proceedings of the National Academy of Sciences of the United States of America*, 115(6), 1162–1167. <https://doi.org/10.1073/pnas.1802701115>
- du Plessis, M. D., Swart, S., Biddle, L. C., Giddy, I., Monteiro, P. M. S., Reason, C. J. C., et al. (2022). The daily-resolved Southern Ocean mixed layer: Regional contrasts assessed using glider observations. *Journal of Geophysical Research: Oceans*, 127(4). <https://doi.org/10.1029/2021JC017760>
- Dybwad, C., Assmy, P., Olsen, L. M., Peeken, I., Nikolopoulos, A., Krumpen, T., et al. (2021). Carbon export in the seasonal Sea Ice zone north of svalbard from winter to late summer. *Frontiers in Marine Science*, 7. <https://doi.org/10.3389/fmars.2020.525800>
- Eady, E. T. (1949). Long waves and cyclone waves. *Tellus*, 1(3), 33–52. <https://doi.org/10.3402/tellusa.v1i3.8507>
- Fadeev, E., Rogge, A., Ramondenc, S., Nöthig, E. M., Wekerle, C., Bienhold, C., et al. (2021). Sea ice presence is linked to higher carbon export and vertical microbial connectivity in the Eurasian Arctic Ocean. *Communications Biology*, 4(1255), 1255. <https://doi.org/10.1038/s42003-021-02776-w>
- Fadeev, E., Wietz, M., von Appen, W.-J., Iversen, M. H., Nöthig, E. M., Engel, A., et al. (2021). Submesoscale physicochemical dynamics directly shape bacterioplankton community structure in space and time. *Limnology & Oceanography*, 66(7), 2901–2913. <https://doi.org/10.1002/lno.11799>
- Fox-Kemper, B., Ferrari, R., & Hallberg, R. (2008). Parameterization of mixed layer eddies. Part I: Theory and diagnosis. *Journal of Physical Oceanography*, 38(6), 1145–1165. <https://doi.org/10.1175/2007JPO3792.1>
- Freilich, M. A., & Mahadevan, A. (2021). Coherent pathways for subduction from the surface mixed layer at ocean fronts. *Journal of Geophysical Research: Oceans*, 126(5). <https://doi.org/10.1029/2020JC017042>
- Giddy, I., Swart, S., du Plessis, M. D., Thompson, A. F., & Nicholson, S.-A. (2021). Stirring of sea-ice meltwater enhances submesoscale fronts in the Southern Ocean. *Journal of Geophysical Research: Oceans*, 126(4). <https://doi.org/10.1029/2020JC016814>
- Giering, S. L., Sanders, R., Lampitt, R. S., Anderson, T. R., Tamburini, C., Boutrif, M., et al. (2014). Reconciliation of the carbon budget in the ocean's twilight zone. *Nature*, 507(7493), 480–483. <https://doi.org/10.1038/nature13123>
- Haine, T. W. N. & Marshall, J. (1998). Gravitational, symmetric, and baroclinic instability of the ocean mixed layer. *Journal of Physical Oceanography*, 28(4), 634–658. [https://doi.org/10.1175/1520-0485\(1998\)028<0634:GSABIO>2.0.CO;2](https://doi.org/10.1175/1520-0485(1998)028<0634:GSABIO>2.0.CO;2)
- Hansen, B., & Østerhus, S. (2000). North Atlantic – Nordic seas exchanges. *Progress in Oceanography*, 45(2), 109–208. <https://doi.org/10.1111/j.1751-8369.2001.tb00053.x>
- Hattermann, T., Isachsen, P. E., von Appen, W.-J., Albrechtsen, J., & Sundfjord, A. (2016). Eddy-driven recirculation of Atlantic water in Fram Strait. *Geophysical Research Letters*, 43(7), 3406–3414. <https://doi.org/10.1002/2016GL068323>
- Håvik, L., Pickart, R. S., Våge, K., Torres, D. J., Thurnherr, A. M., Beszczynska-Möller, A., et al. (2017). Evolution of the East Greenland current from Fram Strait to Denmark Strait: Synoptic measurements from summer 2012. *Journal of Geophysical Research: Oceans*, 122(3), 1974–1994. <https://doi.org/10.1002/2016JC012228>
- Hewitt, H. T., Roberts, M., Mathiot, P., Biastoch, A., Blockley, E., Chassignet, E. P., et al. (2020). Resolving and parameterising the Ocean mesoscale in Earth system models. *Current Climate Change Reports*, 6(4), 137–152. <https://doi.org/10.1007/s40641-020-00164-w>
- Hofmann, Z., von Appen, W.-J., & Mathieu, L. (2022). Continuous ocean current profiles measured with 75kHz VMADCP (vessel-mounted Acoustic Doppler Current Profiler) during MERIAN cruise MSM93 in Fram Strait [Dataset]. *PANGAEA*. <https://doi.org/10.1594/PANGAEA.940023>
- Hofmann, Z., von Appen, W.-J., Mathieu, L., Hagemann, J., Engicht, C., Kuhlmeier, D., & Becker, H. (2022). Physical Oceanography measured with CTD on Triaxus topAWI (towed ocean profiler of the AWI) during MERIAN cruise MSM93 [Dataset]. *PANGAEA*. <https://doi.org/10.1594/PANGAEA.940010>
- Hofmann, Z., von Appen, W.-J., & Wekerle, C. (2021). Seasonal and mesoscale variability of the two Atlantic water recirculation pathways in Fram Strait. *Journal of Geophysical Research: Oceans*, 126(7). <https://doi.org/10.1029/2020JC017057>
- Hoppmann, M., von Appen, W.-J., Hofmann, Z., Mathieu, L., Hagemann, J., Engicht, C., & Kuhlmeier, D. (2022). CTD raw data from RV MARIA S. MERIAN cruise MSM93 [Dataset]. *PANGAEA*. <https://doi.org/10.1594/PANGAEA.941682>

- Hosegood, P. J., Nightingale, P. D., Rees, A. P., Widdicombe, C. E., Woodward, E. M., Clark, D. R., & Torres, R. J. (2017). Nutrient pumping by submesoscale circulations in the Mauritanian upwelling system. *Progress in Oceanography*, 159, 223–236. <https://doi.org/10.1016/j.pocean.2017.10.004>
- Hoyer, J. L., Le Borgne, P., & Eastwood, S. (2014). A bias correction method for Arctic satellite sea surface temperature observations. *Remote Sensing of Environment*, 146, 201–213. <https://doi.org/10.1016/j.rse.2013.04.020>
- Iversen, M. H., Nowald, N., Ploug, H., Jackson, G. A., & Fischer, G. (2010). High resolution profiles of vertical particulate organic matter export off Cape Blanc, Mauritania: Degradation processes and ballasting effects. *Deep-Sea Research Part I Oceanographic Research Papers*, 57(6), 771–784. <https://doi.org/10.1016/j.dsr.2010.03.007>
- Johnson, L., Lee, C. M., D'Asaro, E. A., Thomas, L. N., & Shcherbina, A. Y. (2020). Restratification at a California current upwelling front. Part I: Observations. *Journal of Physical Oceanography*, 50(5), 1455–1472. <https://doi.org/10.1175/JPO-D-19-0203.1>
- Koenig, Z., Fer, I., Kolás, E., Fossum, T. O., Norgren, P., & Ludvigsen, M. (2020). Observations of turbulence at a near-surface temperature front in the Arctic Ocean. *Journal of Geophysical Research: Oceans*, 125(4). <https://doi.org/10.1029/2019JC015526>
- Kozlov, I. E., & Atadzhanova, O. A. (2022). Eddies in the marginal ice zone of Fram Strait and Svalbard from Spaceborne SAR observations in winter. *Remote Sensing*, 14(134), 134. <https://doi.org/10.3390/rs14010134>
- Lavelle, J., Tonboe, R., Tian, T., Pfeiffer, R.-H., & Howe, E. (2016). Product user manual for the OSI SAF AMSR-2 global Sea Ice concentration - Product OSI-408. *Ocean and Sea Ice Satellite Application Facilities*. Retrieved from https://osisaf-hl.met.no/sites/osisaf-hl.met.no/files/user_manuals/osisaf_cdop2_ss2_pum_amsr2-ice-conc_v1p1.pdf
- Lévy, M., Bopp, L., Karleskind, P., Resplandy, L., Ethe, C., & Pinsard, F. (2013). Physical pathways for carbon transfers between the surface mixed layer and the ocean interior. *Global Biogeochemical Cycles*, 27(4), 1001–1012. <https://doi.org/10.1002/gbc.20092>
- Lévy, M., Franks, P. J., & Smith, K. S. (2018). The role of submesoscale currents in structuring marine ecosystems. *Nature Communications*, 9(4758), 4758. <https://doi.org/10.1038/s41467-018-07059-3>
- Llort, J., Langlais, C., Mateau, R., Moreau, S., Lenton, A., & Strutton, P. G. (2018). Evaluating Southern Ocean carbon eddy-pump from biogeochemical-Argo floats. *Journal of Geophysical Research: Oceans*, 123(2), 971–984. <https://doi.org/10.1002/2017JC012861>
- MacIntyre, S., Alldredge, A. L., & Gotschalk, C. C. (1995). Accumulation of marine snow at density discontinuities. *Limnology & Oceanography*, 40(3), 449–468. <https://doi.org/10.4319/lo.1995.40.3.0449>
- Mahadevan, A. (2016). The impact of submesoscale physics on primary productivity of plankton. *Annual Review of Marine Science*, 8(1), 161–184. <https://doi.org/10.1146/annurev-marine-010814-015912>
- Mahadevan, A., Pascual, A., Rudnick, D. L., Ruiz, S., Tintoré, J., & D'Asaro, E. A. (2020). Coherent pathways for vertical transport from the surface ocean to interior. *Bulletin of the American Meteorological Society*, 101(11), E1996–E2004. <https://doi.org/10.1175/BAMS-D-19-0305.1>
- Mahadevan, A., & Tandon, A. (2006). An analysis of mechanisms for submesoscale vertical motion at ocean fronts. *Ocean Modelling*, 14(3–4), 241–256. <https://doi.org/10.1016/j.ocemod.2006.05.006>
- Manucharyan, G. E., & Thompson, A. F. (2017). Submesoscale Sea ice-ocean interactions in marginal ice zones. *Journal of Geophysical Research: Oceans*, 122(12), 9455–9475. <https://doi.org/10.1002/2017JC012895>
- Manucharyan, G. E., & Thompson, A. F. (2022). Heavy footprints of upper-ocean eddies on weakened Arctic sea ice in marginal ice zones. *Nature Communications*, 13(2147), 2147. <https://doi.org/10.1038/s41467-022-29663-0>
- Martin, A. P., Lévy, M., van Gennip, S., Pardo, S., Srokosz, M., Allen, J., et al. (2015). An observational assessment of the influence of mesoscale and submesoscale heterogeneity on ocean biogeochemical reactions. *Global Biogeochemical Cycles*, 29(9), 1421–1438. <https://doi.org/10.1002/2015GB005129>
- Mauritzen, C. (1996). Production of dense overflow waters feeding the North Atlantic across the Greenland-Scotland Ridge. Part 1: Evidence for a revised circulation scheme. *Deep-Sea Research Part I Oceanographic Research Papers*, 43(6), 769–806. [https://doi.org/10.1016/0967-0637\(96\)00037-4](https://doi.org/10.1016/0967-0637(96)00037-4)
- McDougall, T. J., & Barker, P. M. (2011). Getting started with TEOS-10 and the Gibbs Seawater (GSW) oceanographic toolbox. *ScorIapso WG*, 127(532), 1–28.
- McWilliams, J. C. (2021). Oceanic frontogenesis. *Annual Review of Marine Science*, 13(1), 227–253. <https://doi.org/10.1146/annurev-marine-032320-120725>
- McWilliams, J. C., Colas, F., & Molemaker, J. (2009). Cold filamentary intensification and oceanic surface convergence lines. *Geophysical Research Letters*, 36(18). <https://doi.org/10.1029/2009GL039402>
- Nayar, K. G., Sharqawy, M. H., Banchik, L. D., & Lienhard V, J. H. (2016). Thermophysical properties of seawater: A review and new correlations that include pressure dependence. *Desalination*, 390, 1–24. <https://doi.org/10.1016/j.desal.2016.02.024>
- Omand, M. M., D'Asaro, E. A., Lee, C. M., Perry, M. J., Briggs, N., Cetinić, I., & Mahadevan, A. (2015). Eddy-driven subduction exports particulate organic carbon from the spring bloom. *Science*, 348(6231), 222–225. <https://doi.org/10.1126/science.1260062>
- OSI-SAF. (2017). Global AMSR Sea Ice concentration - GCOM-W1, EUMETSAT SAF on Ocean and Sea Ice [Dataset]. *EUMETSAT SAF on Ocean and Sea Ice*. https://doi.org/10.15770/EUM_SAF_OSI_NRT_2023
- Oziel, L., Sirven, J., & Gascard, J.-C. (2016). The Barents Sea frontal zones and water masses variability (1980–2011). *Ocean Science*, 12(1), 169–184. <https://doi.org/10.5194/os-12-169-2016>
- Padman, L., & Erofeeva, S. Y. (2004). A barotropic inverse tidal model for the Arctic Ocean. *Geophysical Research Letters*, 31(L02303). <https://doi.org/10.1029/2003GL019003>
- Padman, L., Erofeeva, S. Y., & Howard, S. (2020). AOTIM5: Arctic Ocean Inverse tide model, on 5 kilometer grid, developed in 2004. <https://doi.org/10.18739/A2S17SS80>
- Parkinson, C. L., & DiGirolamo, N. E. (2021). Sea ice extents continue to set new records: Arctic, Antarctic, and global results. *Remote Sensing of Environment*, 267, 112753. <https://doi.org/10.1016/j.rse.2021.112753>
- Richter, M. E., von Appen, W.-J., & Wekerle, C. (2018). Does the East Greenland current exist in the northern Fram Strait? *Ocean Science*, 14(5), 1147–1165. <https://doi.org/10.5194/os-14-1147-2018>
- Schaffer, J., Timmermann, R., Arndt, J. E., Rosier, S. H. R., Aner, P. G. D., Callard, L. S., et al. (2019). An update to Greenland and Antarctic ice sheet topography, cavity geometry, and global bathymetry (RTopo-2.0.4). *PANGAEA*. <https://doi.org/10.1594/PANGAEA.905295>
- Smith, W. H. F., & Wessel, P. (1990). Gridding with continuous curvature splines in tension. *Geophysics*, 55(3), 293–305. <https://doi.org/10.1190/1.1442837>
- Strong, C., & Rigor, I. G. (2013). Arctic marginal ice zone trending wider in summer and narrower in winter. *Geophysical Research Letters*, 40(18), 4864–4868. <https://doi.org/10.1002/grl.50928>

- Stukel, M. R., Song, H., Goericke, R., & Miller, A. J. (2018). The role of subduction and gravitational sinking in particle export, carbon sequestration, and the remineralization length scale in the California Current Ecosystem. *Limnology & Oceanography*, *63*(1), 363–383. <https://doi.org/10.1002/lno.10636>
- Swart, S., du Plessis, M. D., Thompson, A. F., Biddle, L. C., Giddy, I., Linders, T., et al. (2020). Submesoscale fronts in the Antarctic marginal ice zone and their response to wind forcing. *Geophysical Research Letters*, *47*(6). <https://doi.org/10.1029/2019GL086649>
- Thomas, L. N., Tandon, A., & Mahadevan, A. (2008). Submesoscale processes and dynamics. *Geophysical Monograph Series*, *177*, 17–38. <https://doi.org/10.1029/177GM04>
- Thomas, L. N., Taylor, J. R., Ferrari, R., & Joyce, T. M. (2013). Symmetric instability in the Gulf Stream. *Deep-Sea Research Part II*, *91*, 96–110. <https://doi.org/10.1016/j.dsr2.2013.02.025>
- Tippenhauer, S., Janout, M., Chouksey, M., Torres-Valdés, S., Fong, A., & Wulff, T. (2021). Substantial sub-surface chlorophyll patch sustained by vertical nutrient fluxes in Fram Strait observed with an autonomous underwater vehicle. *Frontiers in Marine Science*, *8*(605225). <https://doi.org/10.3389/fmars.2021.605225>
- Tuerena, R. E., Hopkins, J. E., Buchanan, P. J., Ganeshram, R. S., Norman, L., von Appen, W.-J., et al. (2021). An Arctic strait of two Halves: The changing dynamics of nutrient uptake and limitation across the Fram Strait. *Global Biogeochemical Cycles*, *35*(9). <https://doi.org/10.1029/2021GB006961>
- Våge, K., Pickart, R. S., Spall, M. A., Moore, G. W., Valdimarsson, H., Torres, D. J., et al. (2013). Revised circulation scheme north of the Denmark Strait. *Deep-Sea Research Part I Oceanographic Research Papers*, *79*, 20–39. <https://doi.org/10.1016/j.dsr.2013.05.007>
- von Appen, W.-J. (2021). Submesoscale dynamics in Fram Strait, cruise no. MSM93. (Vol. 93; Tech. Rep.). Alfred-Wegener-Institut, Helmholtz-Zentrum für Polar- und Meeresforschung. https://doi.org/10.48433/cr_msm93
- von Appen, W.-J., Hoppmann, M., & Kuhlmeier, D. (2021). Raw data from surface drifters during MERIAN cruise MSM93 [Dataset]. PANGAEA. <https://doi.org/10.1594/PANGAEA.939736>
- von Appen, W.-J., Schauer, U., Hattermann, T., & Beszczynska-Möller, A. (2016). Seasonal cycle of mesoscale instability of the West Spitsbergen Current. *Journal of Physical Oceanography*, *46*(4), 1231–1254. <https://doi.org/10.1175/JPO-D-15-0184.1>
- von Appen, W.-J., Strass, V. H., Bracher, A., Xi, H., Hörstmann, C., Iversen, M. H., & Waite, A. M. (2020). High-resolution physical-biochemical structure of a filament and an eddy of upwelled water off northwest Africa. *Ocean Science*, *16*(1), 253–270. <https://doi.org/10.5194/os-16-253-2020>
- von Appen, W.-J., Waite, A. M., Bergmann, M., Bienhold, C., Boebel, O., Bracher, A., et al. (2021). Sea-ice derived meltwater stratification slows the biological carbon pump: Results from continuous observations. *Nature Communications*, *12*(7309), 7309. <https://doi.org/10.1038/s41467-021-26943-z>
- von Appen, W.-J., Wekerle, C., Hehemann, L., Schourup-Kristensen, V., Konrad, C., & Iversen, M. H. (2018). Observations of a submesoscale cyclonic filament in the marginal ice zone. *Geophysical Research Letters*, *45*(12), 6141–6149. <https://doi.org/10.1029/2018GL077897>
- Wang, T., Zhao, S., Zhu, L., McWilliams, J. C., Galgani, L., Amin, R. M., et al. (2022). Accumulation, transformation and transport of microplastics in estuarine fronts. *Nature Reviews Earth & Environment*, *3*(11), 795–805. <https://doi.org/10.1038/s43017-022-00349-x>
- Wekerle, C., Hattermann, T., Wang, Q., Crews, L., von Appen, W.-J., & Danilov, S. (2020). Properties and dynamics of mesoscale eddies in Fram Strait from a comparison between two high-resolution ocean–sea ice models. *Ocean Science*, *16*(5), 1225–1246. <https://doi.org/10.5194/os-16-1225-2020>
- Wulff, T., Bauerfeind, E., & von Appen, W.-J. (2016). Physical and ecological processes at a moving ice edge in the Fram Strait as observed with an AUV. *Deep-Sea Research Part I*, *115*, 253–264. <https://doi.org/10.1016/j.dsr.2016.07.001>
- Yankovsky, E., Legg, S., & Hallberg, R. (2021). Parameterization of submesoscale symmetric instability in dense flows along topography. *Journal of Advances in Modeling Earth Systems*, *13*(6). <https://doi.org/10.1029/2020MS002264>
- Zhang, J., Zhang, Z., & Qiu, B. (2023). Parameterizing submesoscale vertical buoyancy flux by simultaneously considering baroclinic instability and strain-induced frontogenesis. *Geophysical Research Letters*, *50*(8). <https://doi.org/10.1029/2022GL102292>
- Zhao, M., Timmermans, M.-L., Cole, S. T., Krishfield, R., Proshutinsky, A. Y., & Toole, J. (2014). Characterizing the eddy field in the Arctic Ocean halocline. *Journal of Geophysical Research: Oceans*, *119*(12), 8800–8817. <https://doi.org/10.1002/2014JC010488>